

Multi-session Localization and Mapping Exploiting Topological Information

Lorenzo Montano-Oliván*, Julio A. Placed, Luis Montano, and María T. Lázaro

Abstract—Operating in previously visited environments is becoming increasingly crucial for autonomous systems, with direct applications in autonomous driving, surveying, and warehouse or household robotics. This repeated exposure to observing the same areas poses significant challenges for mapping and localization —key components for enabling any higher-level task. In this work, we propose a novel multi-session framework that builds on map-based localization, in contrast to the common practice of greedily running full SLAM sessions and trying to find correspondences between the resulting maps. Our approach incorporates a topology-informed, uncertainty-aware decision-making mechanism that analyzes the pose-graph structure to detect low-connectivity regions, selectively triggering mapping and loop closing modules. The resulting map and pose-graph are seamlessly integrated into the existing model, reducing accumulated error and enhancing global consistency. We validate our method on overlapping sequences from datasets and demonstrate its effectiveness in a real-world mine-like environment.

I. INTRODUCTION

Autonomous operation in previously visited regions is essential to many real-world robotic applications. Examples include indoor service robots deployed in specific buildings, infrastructure inspection over time, autonomous warehouse robotics, and multi-agent exploration. While Simultaneous Localization and Mapping (SLAM) focuses on building a map and localizing a robot within it during a single traversal of the environment, such applications require enhanced capabilities for repeated operation in the same regions, revisiting some locations and gathering redundant information multiple times. Multi-session SLAM addresses the challenge of repeated operation in previously visited regions by incrementally building, expanding and refining these maps across sessions. Having accurate, updated maps enables performing downstream tasks more efficiently, and provides the foundation for lifelong SLAM [1]. In particular, multi-session LiDAR (Light Detection and Ranging) mapping has become increasingly important in several domains where constructing high-precision maps is key; including surveying, search and rescue and autonomous driving [2], [3].

This work was partially supported by DGA_FSE T73_23R, the EU project MASTERMINE (HORIZON-CL4-2022-RESILIENCE-01, Grant ID: 101091895), and by project UNDERAIBOT (CPP2022-009792) funded by MICIU/AEI/10.13039/501100011033 and European Union (NextGenerationEU/PTRR).

*Corresponding author.

Lorenzo Montano-Oliván, Julio A. Placed, and María T. Lázaro are with the Instituto Tecnológico de Aragón (ITA), María de Luna 7, Zaragoza, Spain (e-mail: {lmontano, jplaced, mtlazaro}@ita.es).

Luis Montano is with the Instituto de Investigación en Ingeniería de Aragón (I3A), Universidad de Zaragoza, María de Luna 1, Zaragoza, Spain (e-mail: montano@unizar.es).

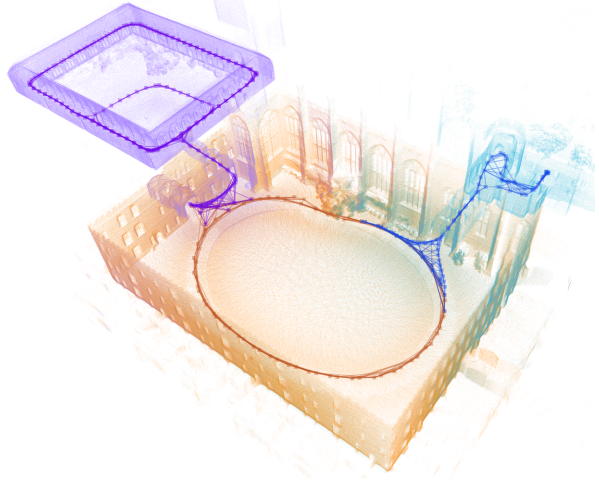


Fig. 1: Map and pose-graph built after processing three overlapping sessions of the Newer College Extension dataset [6] (*Quad M*, *Quad H*, *Cloister*); each depicted in a different color for visualization.

A common approach to multi-session mapping involves executing separate SLAM sessions and subsequently merging the individual maps; this allows for map growth and consistency [4]. However, such process involves generating redundant maps of the same regions and requires an expensive post-processing step to align the full maps. The online alignment between the prior and current maps of the environment in an incremental fashion has also been introduced to link multiple sessions, typically followed by a Pose-Graph Optimization (PGO) that accommodates the inter-session constraints [5]. Nevertheless, these methods still rely on executing time-consuming SLAM algorithms in each session. Moreover, challenges such as drift and insufficient overlap can lead to redundant or inconsistent maps and Pose-Graphs (PGs), and in some cases, unrecoverable states. To reduce computational overhead, the inter-session constraints are often kept sparse, which further limits robustness and scalability.

Map-based localization provides a foundation for an alternative approach to multi-session mapping. Ideally, SLAM would be performed only once to build a high-quality prior map, after which subsequent sessions would rely primarily on localization. In regions not covered by the existing map, mapping and Loop Closing (LC) modules would be selectively activated to expand the environment representation. Building on this concept, we propose a novel approach to facilitate efficient and scalable multi-session localization and mapping, emphasizing the following key aspects:

- We introduce a novel method for determining when mapping is necessary or not by analyzing the underlying PG signature. This results in strongly connected graphs across sessions that improve coherency with respect to sparse inter-session loop closures.
- We develop a multi-session system that integrates such decision-making mechanism to combine state-of-the-art map-based localization with LiDAR mapping.
- We conduct extensive experiments on public datasets, comparing our method against existing multi-session SLAM and localization methods, showing its superior performance. Furthermore, we demonstrate the robustness of the approach through real-world experiments.

II. RELATED WORK

A. Multi-session Mapping

Multi-session capabilities have been extensively studied in the visual SLAM literature. In [5], loop closure factors are employed to jointly optimize multiple graphs (*i.e.*, trajectories) from different sessions. Daoud *et al.* [7] combine multiple maps online by adding these constraints between keyframes with enough similarity. ORB-SLAM Atlas [8] improve the previous by treating the maps as a single entity with a shared descriptor database. In addition, they remove duplicate points, but map merging requires $\approx 13x$ frame rate.

In the domain of LiDAR mapping, where the accuracy and consistency of the maps are crucial, multi-session remains an even more challenging problem. Many works have addressed this problem by creating entirely new maps for each session and combining them either online or offline. LT-Mapper [1] combines multiple maps from independent sessions using ScanContext and Iterative Closest Point (ICP) verification. The constraints are included as anchor node-based inter-session loop factors to reduce the optimization complexity, and rely on a robust back-end to mitigate inevitable false loop detections. In [9], the optimization complexity across sessions is kept bounded through the use of condensed measurements, which enable the merging of local maps upon detecting inter-session loop closures, while simultaneously removing out-dated nodes during the fusion process. Automerge [4] demonstrates large-scale (*i.e.*, hundreds of km) map merging. However, it heavily depends on sufficient overlapping between maps and the availability of Global Navigation Satellite Systems (GNSS) for degraded environments. In addition, the matching complexity scales quadratically with the number of session keyframes, requiring minutes to complete. FRAME [10] employs learned descriptors and place recognition to detect overlap between point cloud maps, boosting the map matching process. Despite this is treated as a triggered event, the events are predefined by the user (*e.g.*, when two robots are nearby). LM-Mapping [2] propose a two-level optimization with local odometry constraints and inter-session factors. Despite this allows to improve local precision and mitigate inter-map inconsistencies, it still requires to rebuild the maps on every session and is relegated to an offline post-processing phase. In MS-Mapping [3], each new LiDAR cloud is registered both sequentially and with

chunks of the prior map, incrementally building the graph and a merged map. Once again, the multi-session mapping problem is formulated as a PGO, where inter-session constraints are modeled as loop closure factors. This approach is shown to outperform direct map-to-map and cloud-to-map registration. LEMON-Mapping [11] presents a scalable multi-robot system that leverages geometric constraints from overlapping point clouds to strengthen the role of inter-session LC. Reliable loop selection and joint inter-session (hierarchical) PGO are shown to be crucial for mitigating map divergence across sessions.

The proposed system is aligned with [3]. Unlike to other related work, we avoid the costly construction, maintenance and matching of complete maps in revisited regions —we only keep a local *submap*. Instead, we only perform mapping and LC for new regions and ensure strong connections with the existing ones. Following [10], we treat this as a triggered event; however, in our case, it is not user-defined but occurs automatically.

B. Map-based Localization

The problem of multi-session mapping is closely related to the *kidnapped robot problem* [12], where the goal is to estimate the robot’s pose given a prior map and no *a priori* information about its location within it. In such cases, map-based localization emerges as a promising solution, despite its accuracy is limited to prior map precision. G-Loc [13] presents a robust PG-based method to LiDAR-inertial localization using prior topological and metric information. However, its operation in unmapped regions is limited and it does not incorporate a way to expand the prior map. LTA-OM [14] first triggers a localization method and then loads the prior map into the odometry module [15], thus not requiring additional map merging operations nor rebuilding a map when operating in the same area. In contrast to [13] and [14], this work addresses the challenge of expanding the prior map by adding robust and dense connections between the current and previous sessions. Furthermore, our approach does not specifically require the prior models to be generated using our SLAM algorithm, as is the case in [14].

C. Pose-graph Connectivity as Quality Measure

The use of topological information has recently gained interest in the robotics community, especially since modern detailed and rich representations call for hierarchical and efficient ways of measuring the quality of the SLAM estimates. The impact of the connectivity of PGs into the estimation problem is well-known [16]. In [17], the intuition behind this link is first formalized relating different graph connectivity indices to estimation reliability. Plated and Castellanos [18] relate the so-called *optimality criteria* to the weighted connectivity of PGs in which edges are weighted with a scalar function of the Fisher Information Matrix (FIM) they encode (*e.g.*, its trace). This allows to efficiently make an uncertainty-aware assessment of the quality of the SLAM estimates, with direct application to active perception.

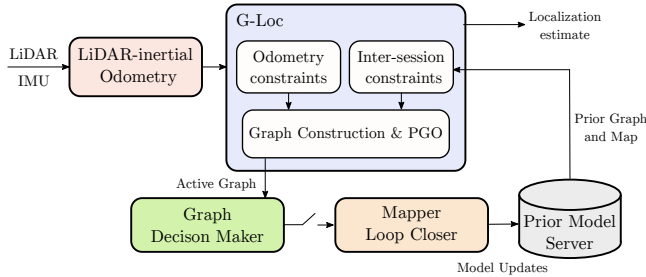


Fig. 2: Overview of the proposed method.

Despite growing interest, these metrics have not yet been used to inform multi-session mapping.

III. METHOD

We propose a graph-based localization method tailored to support multi-session operation, which selectively activates mapping and LC modules to incorporate unvisited regions into the reference model. It features a novel decision-making module that evaluates the connectivity of the underlying joint PG online to determine whether the system should execute map-based localization or augment the map with new information. Additionally, the algorithm includes a robust LC module that efficiently searches for both intra- and inter-session constraints, thereby ensuring accuracy and global consistency across sessions. See Fig. 1.

A. Multi-session Graph Localization

The backbone of the proposed method is G-Loc [13], a robust and precise map-based localization algorithm that combines LiDAR-inertial Odometry (LIO) and map matching constraints into a multiple graph optimization framework. Fig. 3 depicts the different graphs involved in the localization process. First, LIO hyper-edges and cloud-to-cloud matching are optimized within a sliding-window fashion (gray graph in that figure), producing coarse estimates of the robot poses at high frequency (up to IMU rate). A marginalization prior is used to retain information from past states outside the optimization window.

The *active graph* (blue) contains vertices that encode a sparse subset of the LIO states, *i.e.*, LIO-optimized poses of the most recent n key frames, $\mathcal{T} \triangleq \{\mathbf{T}_1, \dots, \mathbf{T}_n \mid \mathbf{T}_i \in SE(3)\}$, together with their associated submaps. Such vertices are connected consecutively via submap-to-submap matching constraints. In addition, this graph includes inter-session constraints (submap-to-map matching) that link \mathcal{T} with nearby vertices of the *reference graph* (orange) and their k -neighbors. The active graph is optimized to obtain a precise localization, keeping the nodes from the reference graph fixed, *i.e.*,

$$\mathcal{T}^* = \operatorname{argmin}_{\mathcal{T}} \left(\sum_{(i,j) \in \mathcal{E}_{\text{intra}}} \|\mathbf{e}_{i,j}^{\text{intra}}\|^2 + \sum_{(i,r) \in \mathcal{E}_{\text{inter}}} \|\mathbf{e}_{i,r}^{\text{inter}}\|^2 \right), \quad (1)$$

where $\|\mathbf{e}\|^2 \triangleq (\mathbf{e}^T \Sigma^{-1} \mathbf{e}) \in \mathbb{R}$ is the quadratic error for a measurement with covariance Σ , $\mathbf{e}_{i-1,i}^{\text{intra}} \in \mathfrak{se}(3)$ are the residuals

associated with consecutive submap matching (intra-session constraints), and $\mathbf{e}_{i,r}^{\text{inter}} \in \mathfrak{se}(3)$ are those associated with the correspondences between current observations and the reference map (inter-session constraints). The pair set $\mathcal{E}_{\text{intra}} \triangleq \{(i,j) \mid 1 \leq i < j \leq n, j = i + 1\}$ and $\mathcal{E}_{\text{inter}} \triangleq \{(i,r) \mid 1 \leq i \leq n, r \in \mathcal{I}_{\text{ref}}\}$, with \mathcal{I}_{ref} the index set of vertices that belong to the reference graph.

Solving (1) enables limited spatial and topological association with previous sessions. G-Loc treats the reference model (PG and point cloud submaps) as a passive input—immutable information used solely for localization. This approach underutilizes the rich information encoded in the PG, including its representation of uncertainty. To address this, we extend [13] by transforming the reference model into an active component of the localization pipeline: when the system traverses an unseen or poorly mapped area, the model is incrementally updated with new observations. See the bottom stream in Fig. 2.

First, all vertices together with their associated submaps that leave the sliding window of key frames (\mathcal{T}) are retained. To bound memory usage, temporal and graph-distance limits are imposed, pruning elements that exceed them. When the mapping mode is triggered by the decision-making module (described in Section III-B), these inactive nodes are selected to form the *candidate graph* (green in Fig. 3), which is then merged into the reference model. As they enter the reference graph, they are automatically incorporated into a LC database. Robust LC search and matching occurs in a separate thread, improving the overall connectivity and accuracy. Therefore, under this mapping mode, the optimization problem (1) becomes:

$$\{\mathcal{T}, \mathcal{R}\}^* = \operatorname{argmin}_{\{\mathcal{T}, \mathcal{R}\}} \left(\sum_{(i,j) \in \mathcal{E}_{\text{intra}}} \|\mathbf{e}_{i,j}^{\text{intra}}\|^2 + \sum_{(i,r) \in \mathcal{E}_{\text{inter}}} \|\mathbf{e}_{i,r}^{\text{inter}}\|^2 + \sum_{(r,s) \in \mathcal{E}_{\text{LC}}} \|\mathbf{e}_{r,s}^{\text{LC}}\|^2 \right), \quad (2)$$

where $\mathcal{R} \triangleq \{\mathbf{T}_r \in SE(3) \mid r \in \mathcal{I}_{\text{ref}}\}$ denotes the set of reference poses, which in mapping mode can grow over time and are jointly optimized together with \mathcal{T} . Note that global PGO is now performed, taking into account both the current and reference poses. In addition, $\mathbf{e}_{r,s}^{\text{LC}} \in \mathfrak{se}(3)$ are the residuals from LC constraints and $\mathcal{E}_{\text{LC}} \triangleq \{(r,s) \mid r, s \in \mathcal{I}_{\text{ref}}, r \neq s\}$.

B. Decision Making

The decision of whether to localize on the previous map or extend it is guided by the topology of the active and reference graphs. Intuitively, if these two graphs are disconnected, this suggests that either the system is entering an unvisited area or the overlap between the observations is insufficient—both scenarios where mapping becomes necessary. Moreover, the system can identify regions with highly uncertain connections, in which case reinforcing the map is also desirable.

1) *On the Graph Signatures:* The structural patterns, or *signatures*, of PGs reflect the conditioning of the underlying optimization problem and can thus serve as measures of the estimation accuracy [17]. For instance, well-distributed

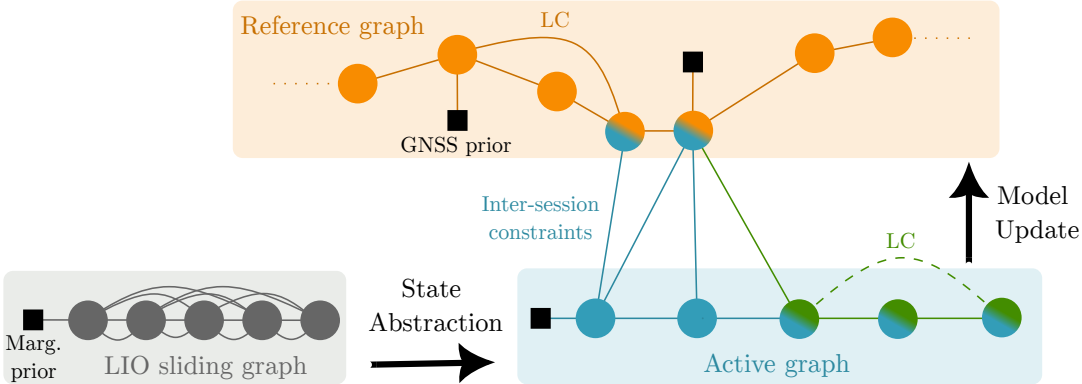


Fig. 3: Visualization of the different graphs used in the multi-session approach. The active graph (blue) is constructed from selected key frames from the odometry graph (gray) along with their condensed measurements, as well as vertices from the reference graph (orange) that are connected via inter-session correspondences. When triggered by the topological decision-making module (*e.g.*, in unmapped regions), a subset of the active graph (candidate graph, green) is integrated into the reference model. Finally, LC and global PGO are performed to reconcile measurements across sessions and ensure consistency.

and broadly spanning loops enhance global consistency, whereas sparse and weakly connected structures can be related to drift, poor conditioning and solution instability. The Laplacian matrix of a graph, $\mathbf{L} \in \mathbb{R}^{m \times m}$ with m the amount of vertices, provides a compact algebraic representation of its topology. In particular, the spectrum of \mathbf{L} encodes fundamental structural properties, with eigenvalues $\lambda = (\lambda_1 = 0, \lambda_2, \dots, \lambda_m)$ when the graph is connected. Among the various metrics derived from spectral graph theory, the average node degree, d , is one of the simplest and most widely used. It reflects the mean connectivity and can be formally defined as:

$$d \triangleq \frac{1}{m} \sum_{k=2}^m \lambda_k. \quad (3)$$

Intuitively, d just captures the ratio between the number of observations and the number of optimization variables (*i.e.*, robot poses). Consequently, PGs with higher ratios yield larger values of d , which correspond to denser connectivity and, in general, more reliable estimation performance. Another fundamental metric is the Fiedler value, λ_2 , *i.e.*, the second-smallest eigenvalue of \mathbf{L} . It reflects how well-connected a graph is: it is strictly positive if and only if the graph is connected, and larger values imply stronger connectivity and improved robustness against partitioning.

Nevertheless, such metrics offer only a limited view of estimation accuracy. For instance, two graphs with same number of edges and vertices yield the same value of d , regardless of whether the edges connect consecutive nodes or form loops. Moreover, the previous indices do not capture uncertainty in the observations. To overcome this limitation, the use of *weighted* connectivity indices has been proposed [18], relating them to optimality criteria. By assigning each edge a weight based on a measure of the uncertainty it encodes (*e.g.*, trace, minimum eigenvalue), one can compute the weighted node degree and the weighted Fiedler value, which approximate T- and E-optimality, respectively.

2) *Two-step Consensus*: Topological metrics of the PG are useful indicators of the graph connectivity and the estimates

accuracy. By tracking their evolution over time, it is possible to anticipate disconnections and determine weakly connected and uncertain regions, *i.e.*, when the reference model needs to be updated. Let us consider the joint PG formed by the active and reference graphs (blue and orange in Fig. 3) from which we can generate two weighted graphs where edges are weighted with the trace and minimum eigenvalue, respectively, of the Information matrix encoded by each edge. The first graph will be used to compute the weighted connectivity index \bar{d} , and the second to compute $\bar{\lambda}_2$.

The objective of the two-step consensus strategy is to enable automatic switching between mapping and map-based localization modes based on the evolution of \bar{d} and $\bar{\lambda}_2$.

Given the quick computation of \bar{d} , we first evaluate its deviation w.r.t. its moving average. Using the moving average rather than a fixed value allows to account for the specifics of the prior model, the algorithm configuration, the current observations, etc. If \bar{d} deviates more than 2σ from the mean, we compute $\bar{\lambda}_2$. If $\bar{\lambda}_2 = 0$, we immediately trigger mapping, since this condition indicates a disconnection between the active and reference graphs (due to matching failures caused by either poorly mapped regions or the presence of new areas). Furthermore, if $\bar{\lambda}_2 > 0$ but \bar{d} decreases beyond 4σ , we also trigger mapping. This situation is related to weakly connected regions or edges carrying limited information, cases in which reinforcing the prior model is also desired. Conversely, while in mapping mode, an increase of \bar{d} back within the confidence bounds together with a recovery of $\bar{\lambda}_2 > 0$ indicates the re-establishment of reliable structural information, thereby triggering a switch to map-based localization. To prevent weak inter-session constraints, we enforce this two-step validation rather than relying solely on $\bar{\lambda}_2 > 0$.

We present Fig. 4 to illustrate the evolution of the topological metrics that drive the decision-making mechanism. We use two partially-overlapping sequences of the New College datasets [19], [6]. For the purpose of analyzing the behavior of the weighted indices, mapping mode is not triggered —focus solely on when it should be activated

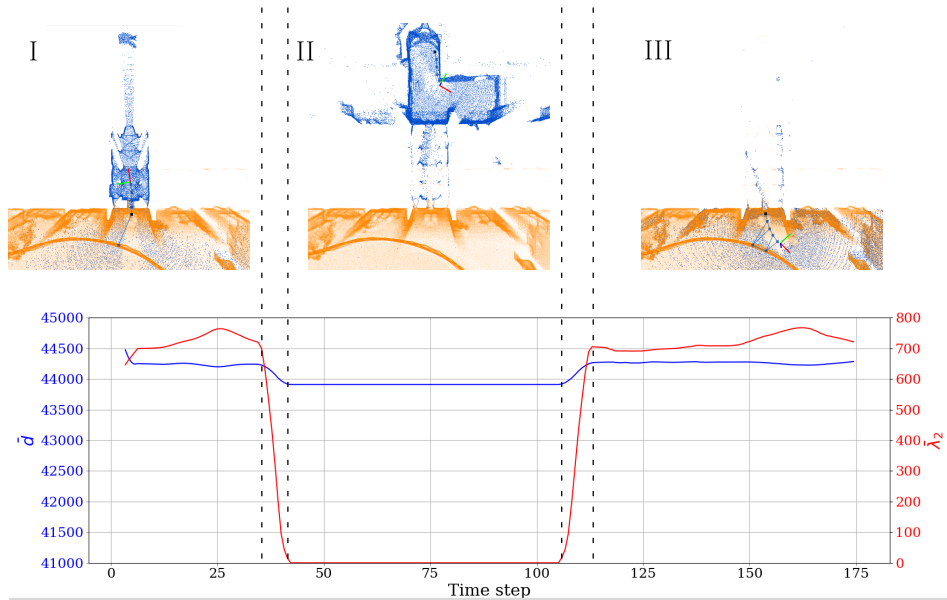


Fig. 4: Illustration of the evolution over time of the weighted connectivity indices (blue: \bar{d} , red: $\bar{\lambda}_2$) during the traversal of previously unmapped regions. *Stage I* corresponds to traversal within previously mapped regions, where localization is performed. *Stage II* indicates entry into unmapped regions, resulting in disconnection between the reference and active graphs, and necessitating mapping. *Stage III* marks reconnection with the prior model and re-establishes map-based localization. The topmost images illustrate examples of these phases: the orange map and PG are the reference model, while the blue ones correspond to the online point cloud and sliding graph.

and deactivated. A reference map (teal point cloud in that figure) of an outdoor region is provided to the algorithm. In stage I, the robot navigates within the mapped region, maintaining stable connectivity indices determined by the sliding graph (blue) configuration and the reference graph (orange) connectivity. At some point, the robot exits the outdoor region and enters an unknown indoor corridor (upper part in Fig. 4). As the robot transitions from stage I to II, the sliding graph gradually disconnects from the prior model: both \bar{d} and $\bar{\lambda}_2$ decrease. During II, the graph remains disconnected (as mapping is not activated), with $\bar{\lambda}_2 = 0$. Finally, the robot returns to the mapped region, transitioning to stage III and reconnecting the sliding graph with the prior model: \bar{d} increases to values akin to those before disconnection and $\bar{\lambda}_2 > 0$.

IV. EXPERIMENTS

In order to validate the proposed method, we have conducted two sets of experiments. The first utilizes two widely used datasets to evaluate the performance of our system in a controlled setting, enabling comparison against existing approaches and a detailed analysis. The second experiment involves a real-world deployment in an underground mine, aimed at demonstrating the system's robustness and application in challenging environments. All experiments were performed on a system equipped with an Intel Core Ultra 7 155H processor and an NVIDIA GeForce RTX 4070 GPU.

A shared requirement for all experiments is the availability of prior topological and geometric models of the environment (*i.e.*, a PG and a point cloud). To fulfill this requirement, we use LG-SLAM [20], a robust and accurate framework for LiDAR-inertial mapping.

A. Dataset Evaluation

The Newer College (NC) [19] and Newer College Extension (NCE) [6] datasets contain different collections of data recorded using a handheld device in diverse environments. In the former, data was recorded using an Ouster OS1-64 LiDAR and its internal Inertial Measurement Unit (IMU). For the latter, an Ouster OS0-128 and an Alpasense Core IMU were used instead. In addition, the datasets contain ground-truth trajectories. Across the two datasets, there exists a series of sequences with partially overlapping trajectories and that have been previously used for multi-session SLAM evaluation [3], [21].

The experiment consisted of gradually processing five overlapping sequences from NC and NCE. First, we create a base model with *Quad-e* (orange in Figs. 1 and 5). Then, we perform incremental updates using the *Quad H* (teal), *Cloister* (purple), and *Short* (blue) sequences, each of which extends the information provided by the preceding one. Fig. 5 illustrates the joint model after processing all sequences. Each new region is shown in a different color, showcasing the contribution of each session, the strong inter-session links, and the fact that overlapping regions are modeled only once.

To evaluate the performance of the proposed method, we present the Absolute Trajectory Error (ATE) Root Mean Squared Error (RMSE) for each individual sequence, and compare our approach with state-of-the-art LIO/SLAM [20], [22], [23] methods (which build separate maps for each sequence) and map-based localization systems [13], [24] (all of them using *Quad-e* as reference map). Note that, in contrast, our method concatenates the sessions and incrementally leverages the information from previous sequences. The re-

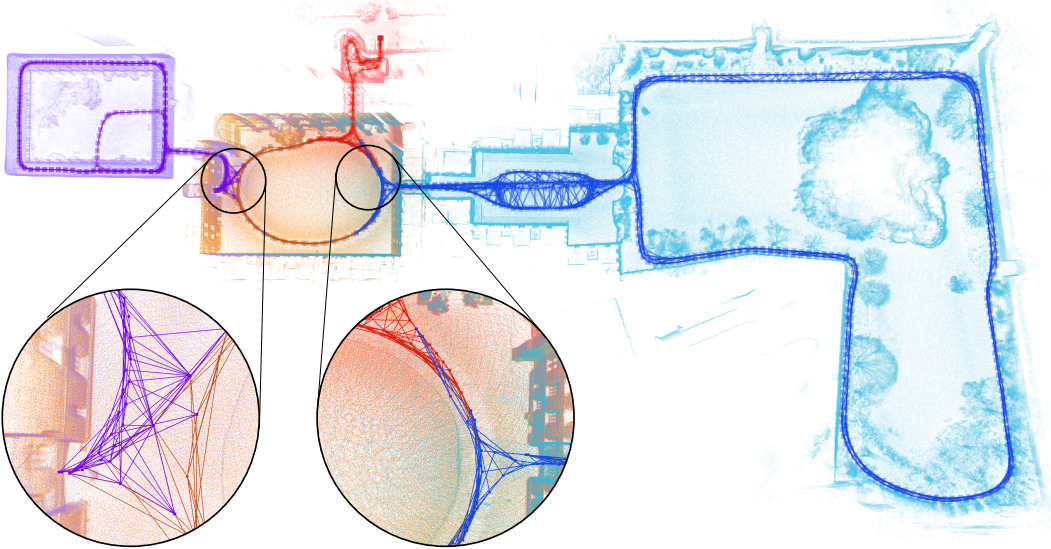


Fig. 5: Multi-session mapping results in NC and NCE datasets: *Quad-e* (orange), *Quad-m* (teal), *Quad-h* (red), *Cloister* (purple), and *Short* (blue). Notably, overlapping regions are modeled only once (both in the map and the PG).

Method / Sequence		<i>Quad-e</i>	<i>Quad-m</i>	<i>Quad-h</i>	<i>Cloister</i>	<i>Short</i>	Avg.
SLAM	LIO-SAM [22]	<u>0.074</u>	0.067	0.13	0.074	<u>0.41</u>	<u>0.15</u>
	NV-LIOM [23]	0.076	0.076	0.18	0.077	0.48	0.18
	LG-SLAM [20]	0.066	<u>0.072</u>	0.090	<u>0.076</u>	0.38	0.14
Map-based Localization	HDL-Loc [24]	–	0.10	×	×	×	×
	G-LOC [13]	–	0.067	<u>0.087</u>	0.21	1.61	0.39
Ours		0.066	0.067	0.082	0.077	0.43	0.14

TABLE I: ATE RMSE (m) in NC and NCE dataset. SLAM methods build separate maps for each sequence. Map-based localization methods employ *Quad-e* as reference map. Our method incrementally concatenates sessions (left to right). Best results are bold and second best are underlined. \times indicates an unrecoverable failure.

sults are reported in Table I. Overall, the proposed approach produced the best results for three out of five sequences and had the lowest average RMSE, alongside LG-SLAM. Since the mapping module is similar to that of LG-SLAM, both approaches achieved the same level of accuracy in *Quad-e*, where no prior information was available. Similarly, when the sequences fully overlap (*i.e.*, in *Quad-m*), our method exhibits the same behavior as G-Loc. However, in *Quad-h*, where there is a new indoor region not present in the previous sequences, our method outperforms all others. As this new area is small, G-Loc still performs accurately, demonstrating its robustness even in partially unmapped regions. However, map-based localization methods fail or accumulate drift in *Cloister* and *Short*, as there are large unvisited regions. Notably, our approach achieves accuracy comparable to SLAM methods while substantially reducing graph complexity by alternating between localization and mapping modes, and providing a joint model.

Fig. 6 presents the evolution of graph weighted connectivity indices while processing *Quad-h* sequence (using *Quad-e* as prior model). This figure is similar to Fig. 4, but now we analyze the behavior during operation (*i.e.*, mapping mode is triggered). At the transition from I to II, the mapping/LC

modules establish multiple connections between the active and reference graphs, leading to a slight increase in \bar{d} . At the same time, these connections ensure that the two graphs remain connected (thus $\bar{\lambda}_2 > 0$). The sharp drop in the Fielder value is explained by the fact that the newly explored region is largely separated from the prior model, being physically connected only through a narrow corridor, which reduces the graph's robustness against partitioning. This effect is also illustrated in Fig. 7, where the red edges highlight the weakest structural links between the two sessions. The prior graph is shown in orange, and the newly explored regions in blue; also, node transparency reflects per-node value of \bar{d} . The transition from II to III corresponds to the reconnection phase. On the one hand, the weighted average node degree stabilizes to a value comparable to stage I, with a slight decrease ($\approx 2\%$) attributed to the covariance of the measurements in the new region. On the other hand, $\bar{\lambda}_2$ gradually increases as the links between the two sessions are reinforced, until reaching a plateau. Compared to stage I, the lower plateau value indicates the presence of two more disjoint regions in the graph. In this experiment, the new area is connected to the prior model only through a narrow corridor, which reduces the overall connectivity relative to

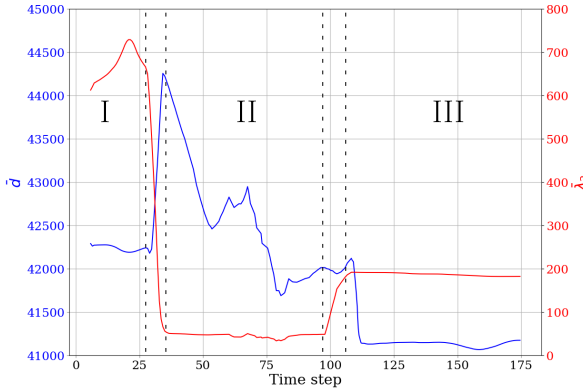


Fig. 6: Evolution of the weighted average node degree (blue) and Fiedler value (red) over time while processing *Quad-h* sequence.

the strongly connected circular trajectory of the reference model (see Fig. 7).

Table II contains a comparison against a multi-session systems in *Parkland* (S1) and *Short* (S2) sequences from [19]. We compare against MS-Mapping [3] and two multi-session localization algorithms (M2F and F2F) reported in [3]. Specifically, M2F localizes the new session point cloud frame-by-frame on the prior map to establish constraints, while F2F localizes frames from the current session against the joint map. The results of M2F and F2F are obtained directly from [3]. The first column reports ATE RMSE after processing each sequence individually, where our approach outperforms the alternatives. The second column shows results when leveraging cross-session information —using *Parkland* while processing *Short*, and vice versa. Results for the combined sequences show comparable results, with lower computational requirements.

Method / Seq.	Individual		Combination	
	S1	S2	S1 (given S2)	S2 (given S1)
M2F (from [3])	0.28	0.46	0.27	0.49
F2F (from [3])	0.28	0.46	0.27	0.50
MS-Mapping [3]	0.26	0.45	0.29	0.40
<i>Ours</i>	0.17	0.38	0.24	0.47

TABLE II: Comparison of ATE RMSE (m) for multi-session approaches on *Parkland* (S1) and *Short* (S2) sequences.

Finally, regarding the execution time, our approach substantially reduces graph complexity by alternating between localization and mapping modes (e.g., the number of nodes of the combined S1 and S2 is 600, whereas the individual S1+S2 is 770). This reduction directly translates into improved computational efficiency, highlighting the benefits of leveraging multi-session information without remapping entire sequences. On average, the proposed method required 50 ms to process each keyframe and 196 ms for LC and PGO. In comparison, the SLAM baseline [20] required 48 ms to process each keyframe and 231 ms for LC and PGO. Notably, in our approach, the LC thread was active only during a part of the sequences, further reducing the overhead compared to SLAM.

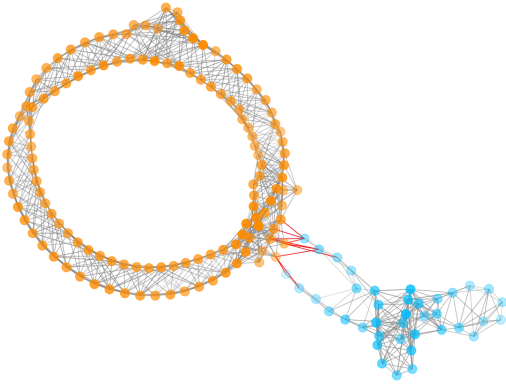


Fig. 7: Visualization of the joint PG after processing *Quad-e* and *Quad-h*. Orange nodes belong to the prior graph (*Quad-e*), while blue ones are the new nodes incorporated to the model during *Quad-h* sequence. Red edges represent the weakest part of the graph.

B. Real-World Experiment

The Kemi Mine is the largest underground mine in Finland, with 1 km depth. The experiments covered a distance of 8 km along a series of spiral primary and secondary galleries. Using a prototype vehicle and following diverse trajectories throughout the tunnels, data from the mine was collected using two Robosense M1 solid state LiDARs and an industrial-grade IMU. In addition, Wi-Fi localization was used to provide a rough location estimate and correctly initialize the map-based localization algorithm, thanks to the large amount of access points located throughout the tunnels.

Fig. 8 contains the resulting map for two of the sequences in the mine, which partially overlap. The prior SLAM-generated model is shown in orange, while the extended model from the second session appears in green. Two areas of the prior map are seamlessly expanded into previously unmapped regions. The PG constructed during the second session exhibits strong internal connectivity, as well as robust links to the prior graph —enabled by the intelligent module responsible for orchestrating mapping and LC operations. Notably, one of the new regions (boxed area in Fig. 8) enforces a loop in the prior map. This clearly improves the overall connectivity of the joint PG. Also, thanks to the global optimization performed where uncertainties of both mapping processes are accommodated, the consistency and precision of the point cloud representation are enhanced.

Specifically, the average node degree of the prior graph (orange graph in Fig. 8) is 5.6. This value increased to 6.5 in the updated graph after processing the second sequence with our multi-session approach (orange and green graphs in the same figure). The analysis of the d is equivalent (2184.6 for the first case, and 2719.9 for the second), indicating the presence of strong inter-session links with low-uncertainty. The weighted number of spanning trees, a measure of global graph connectivity [17], [18], remained nearly constant in both cases (1.4 and 1.3, respectively); this shows that the links between the two sessions did not introduce any significant degradation in graph connectivity. The analysis of the eigenvectors for both graphs reveals that the weakest

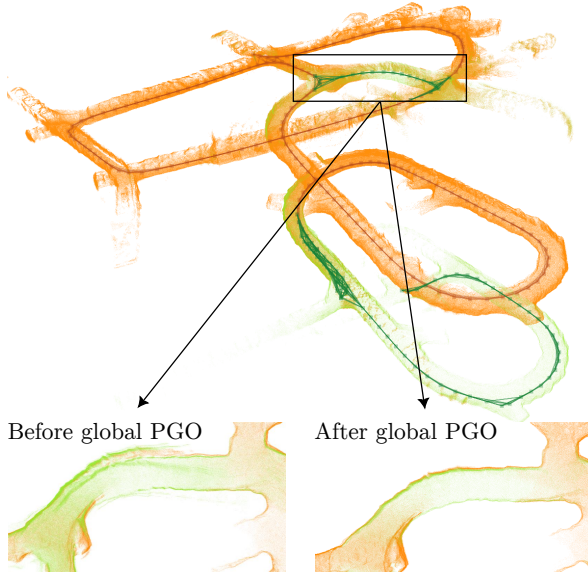


Fig. 8: Multi-session results in the Kemi underground mine. The boxed region shows a loop closure enforced between two areas previously mapped but disconnected. Furthermore, the zoomed-in images further illustrate the impact of global PGO.

region lies within the first session in both cases; *i.e.*, the new session did not introduce any weaker edges. Regarding time consumption, executing SLAM required, on average, 59.9 ms to process each frame (including odometry and mapping). In addition, 149.6 ms were consumed by the LC thread per iteration (including PGO). These values remained similar for both sequences. In contrast, performing our multi-session approach required 45.3 ms to process each frame. Mapping, LC and global PGO were selectively triggered, requiring 109.9 ms on average but being active just 10% of the time.

V. CONCLUSIONS

In this work, we have proposed a novel approach to multi-session LiDAR mapping that extends map-based localization with a decision-making mechanism to selectively trigger mapping and loop closing modules. This allows to avoid redundant mapping of previously visited areas while efficiently incorporating newly explored regions into a common map. Furthermore, the decision process is guided by the connectivity of the underlying pose-graph; this facilitates the construction of robust inter-session connections and accommodating their uncertainty. Future work will focus on efficient, real-time change detection on previously visited areas and its integration into the existing model, strengthening the PG structure when required and enhancing overall mapping.

REFERENCES

- [1] G. Kim and A. Kim, “Lt-mapper: A modular framework for LiDAR-based lifelong mapping,” in *IEEE Int. Conf. on Robotics & Automation*, 2022, pp. 7995–8002.
- [2] C. Pang, Z. Shen, R. Yuan, C. Xu, and Z. Fang, “Lm-mapping: Large-scale and multi-session point cloud consistent mapping,” *IEEE Robotics and Automation L.*, 2024.
- [3] X. Hu, J. Wu, J. Jiao, B. Jiang, W. Zhang, W. Wang, and P. Tan, “Ms-mapping: an uncertainty-aware large-scale multi-session lidar mapping system,” *arXiv preprint arXiv:2408.03723*, 2024.
- [4] P. Yin, S. Zhao, H. Lai, R. Ge, J. Zhang, H. Choset, and S. Scherer, “Automerge: A framework for map assembling and smoothing in city-scale environments,” *IEEE Trans. on Robotics*, vol. 39, no. 5, pp. 3686–3704, 2023.
- [5] B. Kim, M. Kaess, L. Fletcher, J. Leonard, A. Bachrach, N. Roy, and S. Teller, “Multiple relative pose graphs for robust cooperative mapping,” in *IEEE Int. Conf. on Robotics & Automation*, 2010, pp. 3185–3192.
- [6] L. Zhang, M. Camurri, D. Wisth, and M. Fallon, “Multi-camera LiDAR inertial extension to the Newer College dataset,” *arXiv preprint arXiv:2112.08854*, 2021.
- [7] H. A. Daoud, A. Q. Md. Sabri, C. K. Loo, and A. M. Mansoor, “SLAMM: Visual monocular SLAM with continuous mapping using multiple maps,” *PloS one*, vol. 13, no. 4, p. e0195878, 2018.
- [8] R. Elvira, J. D. Tardós, and J. M. Montiel, “ORB-SLAM-Atlas: a robust and accurate multi-map system,” in *IEEE/RSJ Int. Conf. on Intelligent Robots and Systems*, 2019, pp. 6253–6259.
- [9] M. T. Lázaro, R. Capobianco, and G. Grisetti, “Efficient long-term mapping in dynamic environments,” in *IEEE/RSJ Int. Conf. on Intelligent Robots and Systems*, 2018, pp. 153–160.
- [10] N. Stathoulopoulos, B. Lindqvist, A. Koval, A.-A. Agha-Mohammadi, and G. Nikolakopoulos, “FRAME: A modular framework for autonomous map merging: Advancements in the field,” *IEEE Trans. on Field Robotics*, vol. 1, pp. 1–26, 2024.
- [11] L. Wang, X. Zhong, Z. Xu, K. Chai, A. Zhao, T. Zhao, C. Jiang, Q. Wang, and F. Gao, “LEMON-Mapping: Loop-enhanced large-scale multi-session point cloud merging and optimization for globally consistent mapping,” *arXiv preprint arXiv:2505.10018*, 2025.
- [12] J. McDonald, M. Kaess, C. Cadena, J. Neira, and J. J. Leonard, “Real-time 6-DOF multi-session visual SLAM over large-scale environments,” *Robotics and Autonomous Systems*, vol. 61, no. 10, pp. 1144–1158, 2013.
- [13] L. Montano-Oliván, J. A. Placed, L. Montano, and M. T. Lázaro, “G-Loc: Tightly-coupled graph localization with prior topo-metric information,” *IEEE Robotics and Automation L.*, vol. 9, no. 11, pp. 9167–9174, 2024.
- [14] Z. Zou, C. Yuan, W. Xu, H. Li, S. Zhou, K. Xue, and F. Zhang, “LTA-OM: Long-term association LiDAR–IMU odometry and mapping,” *J. of Field Robotics*, vol. 41, no. 7, pp. 2455–2474, 2024.
- [15] W. Xu, Y. Cai, D. He, J. Lin, and F. Zhang, “Fast-lio2: Fast direct lidar-inertial odometry,” *IEEE Trans. on Robotics*, vol. 38, no. 4, pp. 2053–2073, 2022.
- [16] T. Bailey and H. Durrant-Whyte, “Simultaneous localization and mapping (SLAM): Part II,” *IEEE Robotics & Automation Mag.*, vol. 13, no. 3, pp. 108–117, 2006.
- [17] K. Khosoussi, M. Giamou, G. S. Sukhatme, S. Huang, G. Dissanayake, and J. P. How, “Reliable graphs for SLAM,” *Int. Journal of Robotics Research*, vol. 38, no. 2–3, pp. 260–298, 2019.
- [18] J. A. Placed and J. A. Castellanos, “A general relationship between optimality criteria and connectivity indices for active graph-SLAM,” *IEEE Robotics and Automation L.*, vol. 8, no. 2, pp. 816–823, 2022.
- [19] M. Ramezani, Y. Wang, M. Camurri, D. Wisth, M. Mattamala, and M. Fallon, “The Newer College dataset: Handheld lidar, inertial and vision with ground truth,” in *IEEE/RSJ Int. Conf. on Intelligent Robots and Systems*, 2020, pp. 4353–4360.
- [20] L. Montano-Oliván, J. A. Placed, L. Montano, and M. T. Lázaro, “From underground mines to offices: A versatile and robust framework for range-inertial SLAM,” in *Iberian Robotics Conf. (ROBOT)*, 2024, pp. 1–8.
- [21] M. Menezes, M. Muñoz, E. Pignaton de Freitas, S. Cheng, A. de Almeida Neto, P. Ribeiro, and A. Oliveira, “A multisession SLAM approach for RatSLAM,” *J. of Intelligent & Robotic Systems*, vol. 108, no. 4, p. 61, 2023.
- [22] T. Shan, B. Englot, D. Meyers, W. Wang, C. Ratti, and D. Rus, “LIO-SAM: Tightly-coupled LiDAR inertial odometry via smoothing and mapping,” in *IEEE/RSJ Int. Conf. on Intelligent Robots and Systems*, 2020, pp. 5135–5142.
- [23] D. Chung and J. Kim, “NV-LIOM: LiDAR-inertial odometry and mapping using normal vectors towards robust SLAM in multifloor environments,” *IEEE Robotics and Automation Letters*, 2024.
- [24] K. Koide, “Real-time 3D localization using a (velodyne) 3D LiDAR,” https://github.com/koide3/hdl_localization, 2018, accessed: 2025.